Impact of seawater equation of state on the simulation of Atlantic Meridional Overturning Circulation

Libin Ma[1,2] · Bin Wang[3] · Xiao Zhang[2]

Abstract

The Atlantic Meridional Overturning Circulation (AMOC) plays a central role in the decadal variability of global and regional climate through changing poleward transport of heat. However, realistic simulation of the AMOC, i.e., its strength and spatial structure, remains a challenge for ocean general circulation models (OGCMs) and coupled climate models. Here, we investigate how the simulated AMOC could be affected by improved accuracy of the seawater equation of state (EOS) with an OGCM. Two EOSs used in this study: the UNESCO EOS80, and the "stiffened" EOS derived from the compressibility of sea water and the UNESCO EOS80. Compared to the model using the UNESCO EOS80, the model using the "stiffened" EOS yields stronger deep convection in the Labrador Sea, the Irminger-Iceland-Scotland Basin, and the Greenland-Iceland-Norwegian (GIN) seas, which leads to an improvement in the simulation of the AMOC: Along 26.5°N, the maximum transport is increased from 14.9 to 17.4 Sv and the interface between the upper clockwise cell and lower counterclockwise cell is deepened from 2.8 to 3.3 km, both matching the observations better. Taken the Labrador Sea as an example, the processes, including both direct and indirect causes, that in part responsible for the improved AMOC are as follows. The use of "stiffened" EOS increases the density throughout the water column and weakens the stability of sea water. Moreover, the enhanced cabbeling and thermobaric effect strengthen the vertical advection, intensifying the deep convection and increasing formation of deep water, which eventually improves the simulation of the AMOC. The intensified AMOC, in turn, speeds up the surface return flow, transporting more warm and saline water to the high latitudes in the North Atlantic, which contributes to the densification of surface water. Similar analyses can be applied to the Iceland-Scotland Basin and GIN seas. Thus, the enhanced deep convection and formation of deep water in the Labrador Sea, as well as in the Iceland–Scotland Basin and GIN seas, improve the simulated AMOC.

✉ Bin Wang
wangbin@hawaii.edu

Libin Ma
malibin109@163.com

1 State Key Laboratory of Severe Disaster, Chinses Academy of Meteorological Sciences, South Zhongguancun Street No. 46, Haidian District, Beijing 100081, China

2 Key Laboratory of Meteorological Disaster of Ministry of Education (KLME)/Joint International Research Laboratory of Climate and Environment Change (ILCEC)/Collaborative Innovation Center on Forecast and Evaluation of Meteorological Disasters (CIC-FEMD), School of Atmospheric Sciences, Nanjing University of Information Science and Technology, Nanjing 210044, China

3 Department of Atmospheric Sciences, International Pacific Research Center, School of Ocean and Earth Science and Technology, University of Hawaii at Manoa, 1860 East-West Road, POST Bldg. 401, Honolulu, HI 96822, USA

1 Introduction

The Atlantic Meridional Overturning Circulation (AMOC) plays a vital role in the variability of global and localized climate because of its effective meridional heat transport. The observed AMOC consists of two opposite meridional circulation cells: an upper clockwise cell that spans from surface to deep ocean (3000–4000 m) and a lower cell which is counterclockwise in the bottom (below 4000 m). The upper cell of the AMOC includes four branches: upwelling of the southward deep water in the Southern Ocean, the surface water transverses northward to the northern high latitudes, the surface water becomes denser and sinks in the regions where deep convection occurs, and the formed deep water moves southward closing the loop, whereas the bottom counterclockwise circulation is related to the Antarctic Bottom Water (AABW) (e.g., Kuhlbrodt et al. 2007). The northward transport of heat flux by the overturning circulation from low latitudes to high latitudes offsets the heating inequity because of the differential radiation over the Earth (Lozier 2012). Without the poleward transport of warm surface water, the surface temperature difference between the polar region and the equator would reach 110 °C, not the current 30 °C (Gill 1982). The AMOC carries 0.5 PW (1 PW $= 10^{15}$W) heat across the equator making the Northern Hemisphere is slightly warmer than Southern Hemisphere, pushing the mean position of the Intertropical Convergence Zone (ITCZ) to the northern side of the equator (Frierson et al. 2013; Marshall et al. 2014). The AMOC modulates the displacement of the ITCZ, e.g., weakening of the AMOC makes the ITCZ move equatorward, and vice versa (e.g., Vellinga and Wood 2002; Zhang and Delworth 2005; Cheng et al. 2007; Liu and Hu 2015; Liu et al. 2017).

The AMOC exerts significant influence on the variations of sea level. By analyzing the numerical results of a climate system model (CSM), Levermann et al. (2005) pointed out that the global sea level rise can be caused by the weakening of the AMOC. Ezer (2013) concluded that the sea level rise along the east coast of the United States is spatially uneven and temporally unsteady, which are related to the AMOC's transport. The weakening of the AMOC first results in the Atlantic Multidecadal Oscillation (AMO) transition to its negative phase (McCarthy et al. 2015), accelerating the sea level rise in the northeast coast of the United States (Boon 2012; Sallenger et al. 2012). Continuous weakening of the AMOC will lead to the sea level rise in the whole globe, including the northeast coast of the United States (e.g., Yin et al. 2009) and high latitudes of the North Atlantic and Southern Ocean (Chen et al. 2019), as revealed by future projection experiments., implying that the variability of AMOC also plays a central role in future climate change (Srokosz et al. 2012; Srokosz and Bryden 2015).

The aforementioned studies suggested the importance of accurately modelling the variability of the AMOC. However, realistically simulating the variability and spatial structure of the AMOC is still a big challenge. By analyzing 20 global ocean-sea ice coupled models from the Coordinated Ocean-Ice Reference Experiments phase II (CORE-II), Danabasoglu et al. (2014) pointed out that all the models have weaker and shallower AMOC in terms of the mean state versus the observation at 26.5°N. In addition, the spatial structures of AMOC's variability and the location of maximum AMOC variability are different among the models of the CORE-II (Danabasoglu et al. 2016). Although having greater mean strength and enhanced variance of the AMOC, compared to the models of the CORE-II, six reanalysis datasets still show diverse spatial structures of the mean state and linear trend (Karspeck et al. 2017). In the context of numerical simulations, the performance of the simulated AMOC is related to atmosphere-ocean-sea ice interaction (e.g., Griffies et al. 2009), spatial resolution (Delworth et al. 2012), and corresponding settings of parameterization (Danabasoglu et al. 2014).

The AMOC variability is sensitive to buoyancy anomalies. A number of numerical models, including CSMs and Earth System Models (ESMs), have been used to study the sensitivity of AMOC's variability to freshwater perturbations. The freshwater perturbations are usually added in the regions of deep convection, such as the Labrador Sea and the Greenland-Iceland-Norwegian (GIN) seas. By adding the freshwater perturbation, the AMOC is weakened, which modulates the global and localized climate variability (e.g., Gao et al. 2003; Kevin 2005; Timmermann et al. 2007; Stammer 2008; Kopp et al. 2010; Stammer et al. 2011), including the paleoclimate (Rahmstorf 2002; Alley et al. 2003; McManus et al. 2004; Lynch-Stieglitz et al. 2007).

Such freshwater perturbations influence the AMOC by modifying the density gradient of surface water. The dilution of surface water by injecting freshwater perturbations strengthens the stratification of water column, hindering the occurrence of deep convection. The reduction of deep-convective occurrence further affects meridional overturning activities, thus the AMOC. This implies that changes in the density in the regions of deep convection play a vital role in the variability of the AMOC. The main objective of the present study is to explore whether different EOS of sea water will affect the simulation of the AMOC via adjusting the density distribution of sea water.

The seawater density in OGCM and CSMs/ESMs is calculated by the EOS of sea water as a function of water temperature, salinity, and pressure. However, most of the existing OGCMs adopt the Boussinesq approximation (e.g., Zeytounian 2003), in which a constant reference density is used in the momentum equations. This approximation causes the so-called Boussinesq error (Dukowicz 2001), which then

induces errors in the computation of pressure-gradient force (PGF). Another error arises from the accompanying approximation in the hydrostatic equation, in which the pressure is considered to be independent of density and a depth-to-pressure conversion function is applied (e.g., Fofonoff and Millard 1983; Jackett and McDougall 1995; Shchepetkin and McWilliams 2011) to linearly solve the hydrostatic equation. This kind of error is called the "density error" (Dewar et al. 1998; Dukowicz 2001). Both errors come from neglecting the compressibility of the sea water.

There are some studies focusing on the reduction of the aforementioned errors. Dewar et al. (1998) argued that the approximation in the hydrostatic equation could attenuate the feedback of the total pressure on density. To reduce the "density error", the authors suggested that the hydrostatic equation should be implicitly solved by a Runge–Kutta method to include the full feedback of pressure on density. Dukowicz (2001), starting from the view of compressibility of seawater, proposed an equivalent but "stiffer" EOS, which aims to reduce the errors in computation of density and PGFs in ocean simulations. It was implemented in the parallel ocean program (POP) model (Smith et al. 2010), which is the ocean component of the Community Climate System Model (CCSM) and Community Earth System Model (CESM) (Hurrel et al. 2013).

The main topic of this study is to investigate the impacts of seawater EOS, including the UNESCO EOS80 and the "Dukowicz stiffened" EOS, on the simulation of AMOC. The precise meaning of the two EOSs will be described in Sect. 2, along with model description and methodology used in this study. In Sect. 3, we present numerical results. Possible physical processes responsible for the changes in the AMOC are also discussed in Sect. 3. Finally, summary and concluding remarks are presented in Sect. 4.

2 Model description and seawater equation of state

2.1 Model description

A stable version of ocean general circulation model (OGCM) NEMO3.4 (Madec 2008) with ORCA1 configuration is used here. This model is the ocean component of many other coupled climate models and is also the Nanjing University of Information Science and Technology Earth System Model Version 3.0 (NESMv3; Cao et al. 2018). The model configuration has horizontally varying resolution of approximated 1° zonally and meridionally and 46 vertical levels with uneven layer thickness. The Louvain-la-Neuve Sea Ice Model version 2 (LIM2), a dynamic sea ice model, is also configured by compiling the package ORCA2_LIM (Fichefet and Maqueda 1997). To account for unresolved eddies, the Redi

isopycnal diffusion (Redi 1982) and the Gent–McWilliams parameterization (Gent and McWilliams 1990) are used with eddy diffusivity of 1000 $m^2 s^{-1}$. The turbulent kinetic energy scheme (Blanke and Delecluse 1993) for vertical diffusivity is used, which has a minimum value of 1.2×10^{-5} m^2 s^{-1}. All climatological forcing fields are repeated annually during model integration; they come from the DRAKKAR forcing set DFS4.4 (Dussin and Barnier 2013). The surface boundary conditions fields are computed using the bulk formulae developed by Large and Yeager (2004) and the atmospheric fields and ocean/sea-ice variables. All simulations start from a resting ocean with climatological temperature and salinity distribution (Levitus 1982). It is worth noting that on the one hand the restoring techniques, such as the restoring strength of surface salinity, are closely linked to the AMOC transports (Griffies et al. 2009; Behrens et al. 2013; Danabasoglu et al. 2014) and on the other hand to additional and artificial adjustment on the seawater hydrographic properties attenuates and restricts the accuracy with respective to the impacts of EOS on the AMOC. Thus, no restoring technique, including the surface salinity restoring, is used in this study. The model is integrated for 500 years, which is able to spin up the deep ocean compared to the 300-year integration by the CORE-II models (Danabasoglu et al. 2014), in each case and the last 10-year output are used to construct monthly mean climatology.

2.2 Two kinds of seawater equation of state

The first EOS used in this study is the one form of the UNESCO EOS80 (UNESCO, 1981) proposed by Jackett and McDougall (1995), in which the density (ρ, kg/m^3) is taken as a function of potential temperature (θ, ℃), salinity (S), and pressure (p, bars) as follows:

$$\rho(\theta, S, p) = \frac{\rho(\theta, S, 0)}{1 - \frac{p}{K(\theta, S, p)}}, \tag{1}$$

where $\rho(\theta, S, 0)$ is the density at the surface of 1 atm pressure fitted by a 15-term polynomial of θ and S; $K(\theta, S, p)$ is a 26-term function in powers of θ, S and p. The corresponding coefficients of (1) used in NEMO3.4 are from Jackett and McDougall (1995).

The other EOS used here is the "stiffened" EOS, which is derived based on the compressibility of seawater (Dukowicz 2001), aiming to reduce the aforementioned Boussinesq and density errors. The density in (1) can be rewritten as

$$\rho = r(p) \times \rho^*_{EOS(\theta, S, p)}, \tag{2}$$

where the multiplier $r(p)$ is independent of the local θ and S, and is selected as a universal function. $\rho^*_{EOS(\theta, S, p)}$ is the thermobaric or "stiffened" density as it depends on

themobaric compressibility [see Dukowicz (2001) for details]. Using (2) one can renormalize pressure as

$$\frac{dp^*}{dp} = \frac{1}{r(p)}. \tag{3}$$

Hence the PGF in the momentum equations, due to Boussinesq approximation and the hydrostatic equation, becomes

$$PGF = \frac{1}{\rho_0}\nabla p^*, \tag{4}$$

and

$$\frac{\partial p^*}{\partial z} = -\rho^* g = -\frac{\rho g}{r(p)}. \tag{5}$$

The scaling factor $r(p)$ and pressure p (e.g., Fofonoff and Millard 1983) are calculated as follows:

$$r(p) = 1.02819 - 2.93161 \times 10^{-4} exp(-0.05p) + 4.4004 \times 10^{-5}p, \tag{6}$$

where the pressure p is in bars, and

$$p(Z) = 0.059808[exp(-0.025Z) - 1] \\ + 0.100766Z + 2.28405 \times 10^{-7}Z^2, \tag{7}$$

where Z is the water depth and unit in meter. It should be pointed out that there is another "stiffened" EOS proposed by Shchepetkin and McWilliams (2011), which is suitable for the terrain-following coordinate (sigma coordinate). However, the z-coordinate is used in the current study. Thus, only the "stiffened" EOS proposed by Dukowicz (2001) is implemented here. The other one will be discussed in the future when we use the sigma coordinate. Usage of the modified ρ^* and p^* reduces the Boussinesq and density errors by an order of magnitude (Dukowicz 2001), which induces associated geostrophic velocities on the order of O (1 cm s^{-1}) (Dewar et al. 1998). This study will validate the benefits by using the "stiffened" EOS and investigate whether it has positive influence on the simulation of the AMOC. Two experiments are thus performed: One uses the UNESCO EOS80, referred to as CTRL, and the other adopts the "stiffened" EOS, referred to as STIF. Moreover, three additional experiments are also conducted by using the "stiffened" EOS to replace the UNESCO EOS80 in specific regions: one is in the tropical Atlantic (15ºS–15ºN and 70ºW–20ºE) (referred to as TALT_STIF), another is in the Labrador Sea (50°N–65°N and 60°W–45°W) (referred to as LABS_STIF), and another is in the South Ocean (75°S–55°S and 0°E–360°E) (referred to as SO_STIF). The sensitivity experiments conducted here aim to investigate whether the changes in stratification in the tropical Atlantic, the Labrador Sea, and South Ocean will affect the variability of the AMOC.

2.3 Methodology

Some basic calculations are adopted in this study. First of all, the heat transport in the Atlantic, which is decomposed into the overturning and gyre components (Bryden and Imawaki 2001; Born et al. 2010), is computed as follows:

$$Q_T = Q_{overturning} + Q_{gyre} \\ = \rho_0 c_p \left(\iint \bar{v}\bar{T}\, dxdz + \iint v'T'dxdz \right), \tag{8}$$

where constants ρ_0 and c_p are the reference density and specific heat capacity of seawater, respectively; $\bar{T}$ and $\bar{v}$ correspond zonal mean potential temperature and meridional velocity in the Atlantic, respectively, with associated deviations (T' and v'). Note that the terms $v'\,\bar{T}$ and $\bar{v}\,T'$do not include during the calculation in (8) because of the secondary contribution relative to other terms and neglect of the cross-scale interactions in this study.

The buoyancy gain, which is related to the stratification, is used to replace the direct analyses of heat flux and freshwater flux (e.g., de Larvengne et al. 2014) and is calculated by using:

$$B_{gain} = \frac{g}{\rho_0} \int_0^{2000} \left[\sigma_0(2000\,\text{m}) - \sigma_0(z)\right]dz, \tag{9}$$

where g and ρ_0 are the acceleration gravity and reference seawater density, respectively; $\sigma_0(z)$ is the potential density relative to the surface. Note that the potential density at the bottom is used to replace the one of $\sigma_0(2000\,\text{m})$ during the calculation when the water column is shallower than 2000 m. The larger buoyancy gain indicates a stronger stratification.

In addition, the subpolar gyre can be represented and evaluated by the barotropic stream function calculated as follows (Marzocchi et al. 2015):

$$\phi_B(x, y) = \int_{x_w}^x \int_{-H}^0 v(x, y, z)dzdx, \tag{10}$$

with the ocean depth H, which is positive upward, of the water column, the meridional velocity $v(x, y, z)$, and the starting point of the integration x_w. The negative and positive streamfunction values denote the anticlockwise subpolar gyre and clockwise subtropical gyre, respectively.

3 Numerical results

3.1 Sensitivity of the AMOC to EOS

The variations of sea surface temperature (SST), sea surface salinity (SSS), and ocean currents are discussed here with the results from two kinds of EOSs (CTRL and STIF). Figure 1 shows the annual mean SST and SSS, and the corresponding differences between CTRL and STIF. The general patterns of SST and SSS in CTRL and STIF are quite similar (Fig. 1a, b, d, e). However, substantial regional differences between the two are obvious. Compared to CTRL, STIF cools surface water in the west of
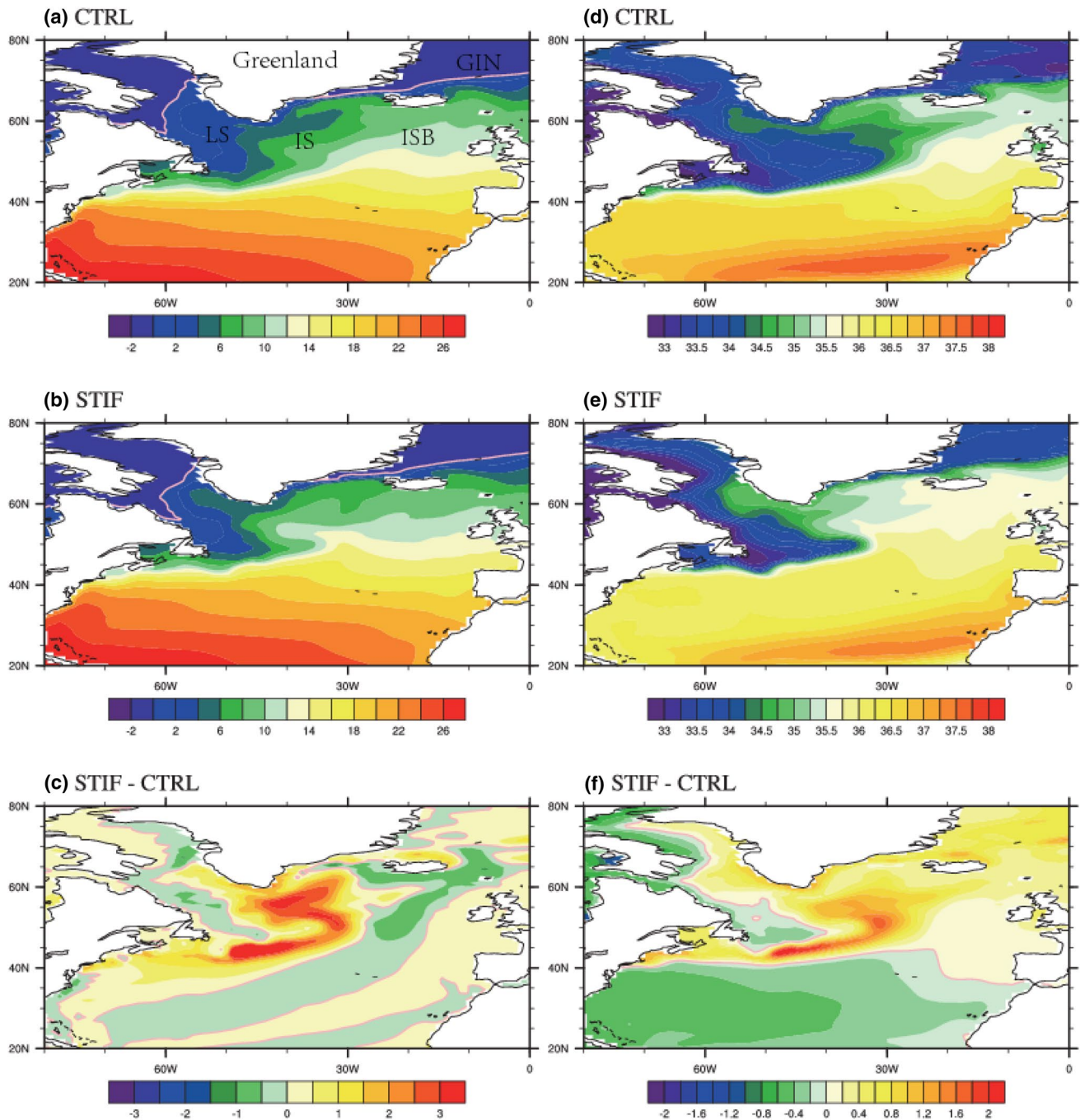

Fig. 1 Annual-mean SST (left panel; °C) and SSS (right panel; psu): **a**, **d** CTRL, **b**, **e** STIF, and **c**, **f** differences between STIF and CTRL. The pink contour denotes the zero isoline. LS, IS, GIN, and ISB in **a** represent the Labrador Sea, Irminger Sea, Greenland–Iceland–Norwegian seas, and Iceland–Scotland Basin, respectively

Labrador Sea and increases the temperatures of surface water in the east of Labrador Sea and in the Irminger Sea (Fig. 1c). SST difference is also found around Iceland with SST being increased and decreased in STIF on the northern and southern sides, respectively. There is no significant SST difference in the subtropical gyre between the two. The difference in SSS is more organized (Fig. 1f). In the subtropical gyre, fresher water is found in STIF compared to CTRL. Oppositely, SSS in the subpolar gyre is increased in STIF, except for the reduction of SSS in the western and southern Labrador Sea. The saltier water found in the northern Labrador Sea implies that there may be stronger deep convection in STIF, which favors the strengthening of the AMOC in the Labrador Sea (e.g., Marshall and Schott 1999; Deshayes et al. 2014).

The surface ocean circulation is discussed here in terms of the ocean currents averaged over the upper 200 m. As shown in Fig. 2a, the modeled Gulf Stream in CTRL detaches the Cape Hatteras and moves to the east; then its extension, the North Atlantic Current (NAC), marches northeast to the south of Iceland. The NAC subsequently splits into two branches: One moves northward west of Iceland, and the other flows southeastward south of Iceland. Moreover, a cyclonic circulation extends from the Labrador Sea to the Irminger Sea, which is the preconditioner for the occurrence of deep convection (e.g., Marshall and Schott 1999). The simulated NAC in STIF is more sharply extending northeastward to 40°W; then, it splits into two branches around 42°W: One extends northwestward into the Irminger Sea, and the other further marches to the south of Iceland (Fig. 2b). Compared to CTRL, STIF shows a constrained cyclonic circulation, which is mainly limited in the Labrador Sea. Regarding the difference, as shown in Fig. 2c, STIF shows stronger ocean currents along the Gulf Stream and NAC, which validates and confirms the conclusion of Dewar et al. (1998) that improved calculation of EOS increases the velocity by several centimeter per second in the dynamically important areas like the western boundary currents. The intensification of the Gulf Stream and NAC suggests that more warm and saline water is transported to the Irminger Sea (e.g., Drews et al. 2015).

In addition to changes in the simulated SST and SSS, the subsurface hydrological properties of seawater are also modified. Figure 3 shows the T–S diagrams averaged over the 100–200 m in the Labrador Sea, the Irminger-Iceland-Scotland Basin, and the Greenland-Iceland-Norwegian (GIN) seas. Generally speaking, the subsurface water reproduced in STIF is denser than that in CTRL. In the Labrador Sea and the GIN seas, more saline water are reproduced in STIF (Fig. 3a, c) indicating that the variability of seawater density in both regions are dominated by the seawater salinity. In addition, the densification of subsurface water in the
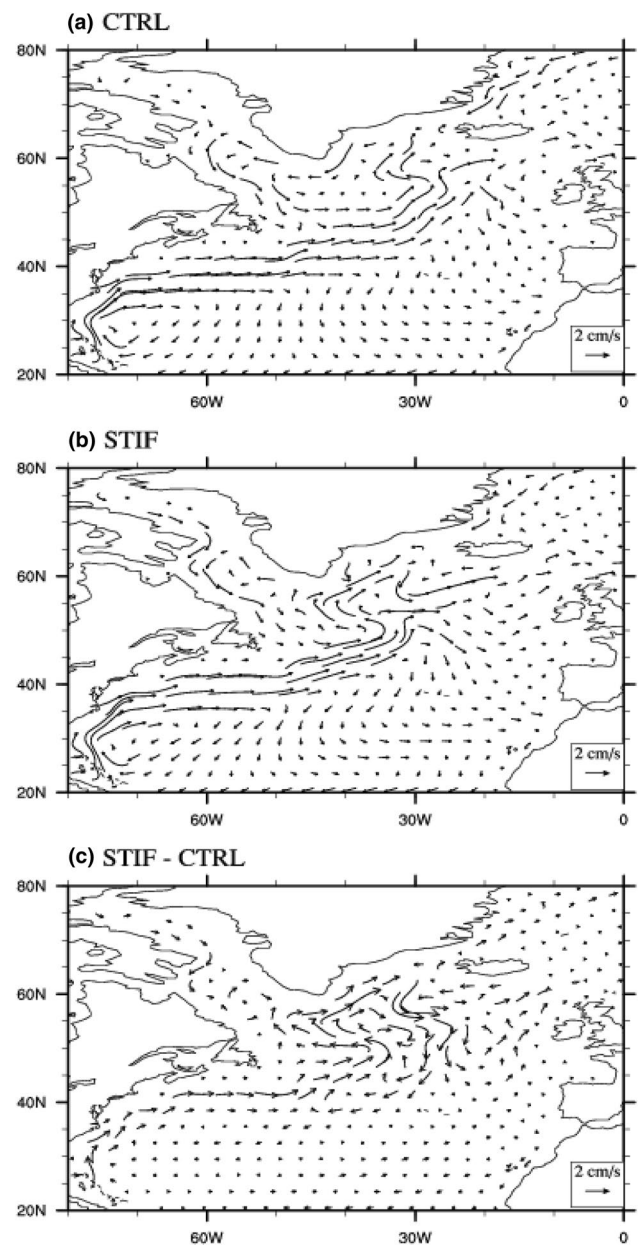

Fig. 2 Annual-mean ocean currents averaged over the upper 200 m (cm s^{-1}): **a** CTRL, **b** STIF, and **c** differences between STIF and CTRL

Labrador Sea is prone to enhance the formation of Labrador Sea water, whilst the densification of subsurface water in the GIN seas tightly relates to the formation of North Atlantic Deep Water (NADW). Moreover, the formed NADW, which also includes the Labrador Sea water, are transported to the Irminger Sea and Iceland basin (Luyten et al.1993; Yashayaev et al. 2007), leading to the blended hydrological properties of sea water in the Irminger–Iceland–Scotland Basin (Fig. 3b).
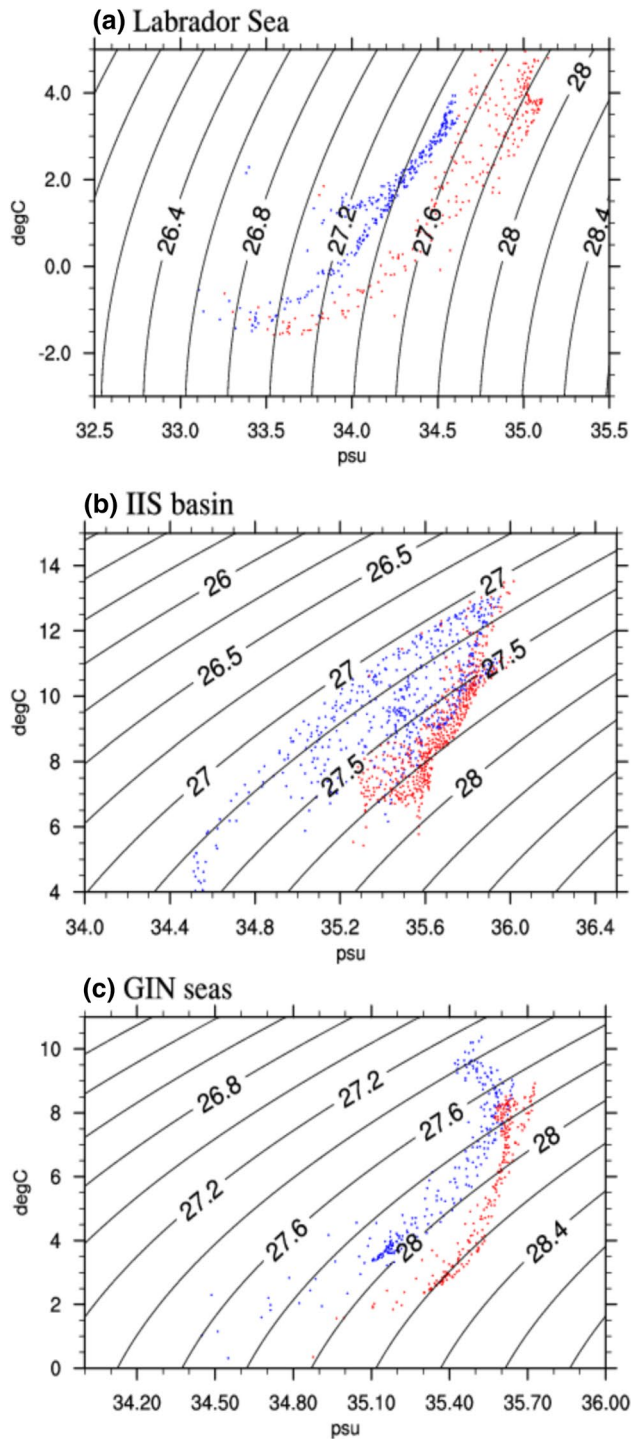
(a) Labrador Sea

(b) IIS basin

(c) GIN seas

Fig. 3 Annual-mean T–S diagrams averaged over 100–200 m in the **a** Labrador Sea (50°N–65°N and 60°W–45°W), **b** Irminger-Iceland-Scotland Basin (50°N–65°N and 35°W–10°W), and **c** the Greenland–Iceland–Norwegian (GIN) seas (60°N–70°N and 20°W–0°W). Blue and red dots represent the results of CTRL and STIF, respectively

(a) CTRL

(b) STIF - CTRL

- Gyre Q
- Overturning Q
- Total Q

Fig. 4 Annual-mean heat transport (PW) in the Atlantic Ocean (black), which is decomposed into overturning (blue) and gyre (red) components in **a** CTRL and **b** the difference between STIF and CTRL

The increased SST in the subpolar gyre domain, as shown in Fig. 1c, is the signature of a stronger ocean heat transport. Figure 4 sho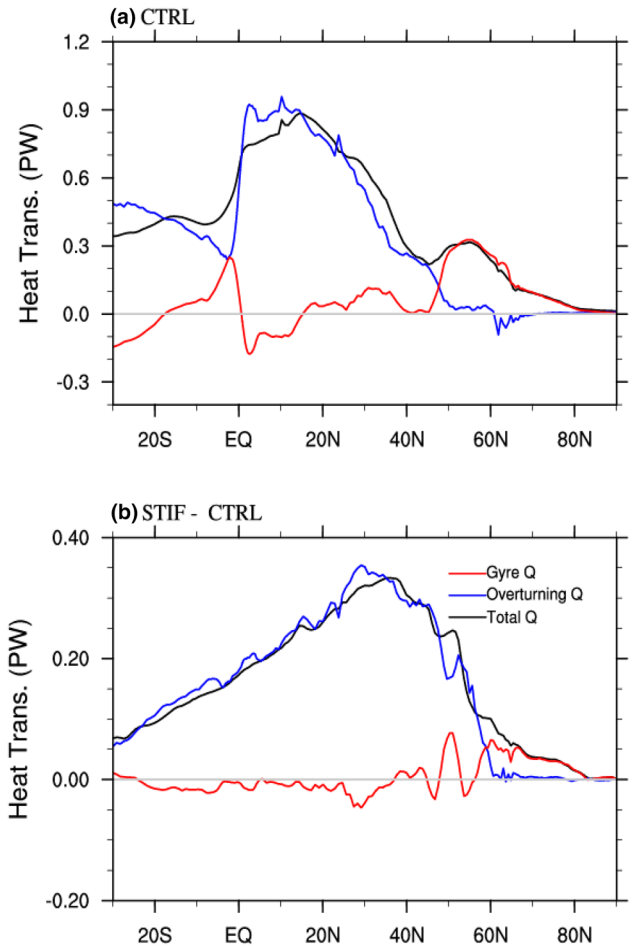ws the annual-mean heat transport in the Atlantic in the two model simulations and their differences. In CTRL, Q_T reaches its peak around 15°N (Fig. 4a). South of 50°N, the overturning heat transport dominates the variation of Q_T, whereas the gyre heat transport determines the Q_T north of 50°N due to the contribution of overturning heat transport being trivial. Compared to CTRL, the oceanic heat transport Q_T is enhanced in STIF, with an increase of 0.35 PW near 35°N (Fig. 4b). In general, the enhancement of Q_T comes from the intensification of overturning heat transport, except at the high latitudes north of 60°N. Note that STIF also shows increased gyre component in the latitudinal range between 40°N and 60°N, which suggests that there is an enhanced subpolar gyre in STIF, compared to CTRL.

In general, both CTRL and STIF capture the main structure of the AMOC, comprising a clockwise circulation above 3000 m and a counterclockwise circulation below 3000 m (Fig. 5a, b). The difference of simulated AMOC can also be differentiated in Fig. 4a, b. Consistent with the enhanced overturning heat transport (Fig. 4b), the AMOC in STIF is
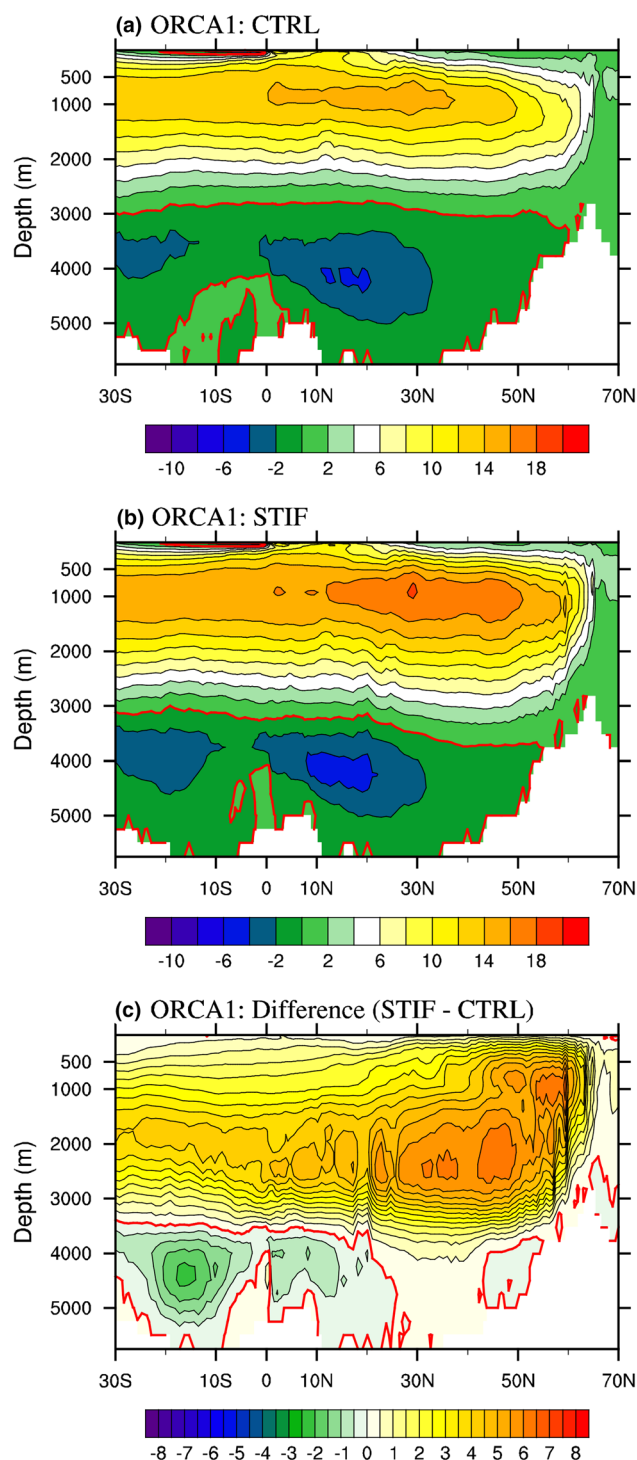
Fig. 5 Annual-mean meridional stream function (units: $Sv = 10^6$ m^3 s^{-1}) of ORCA1: **a, d** CTRL, **b, e** STIF, and **c, f** differences between STIF and CTRL. The thick red contour denotes the zero isoline

deeper than that in CTRL. Moreover, the maximal transport of the AMOC in CTRL is located between 0°N and 40°N, which is smaller than that in STIF located between 10°N and 50°N. The above-mentioned differences in Fig. 5a, b

suggests that there are stronger northward near-surface flow and southward deep flow in STIF (Fig. 5c). The maximum positive difference in the upper layer appears between 50°N and 60°N and centers at 1000-m depth. Then, it gradually deepens and moves southward around 2000-m depth. This implies an enhancement in downwelling in the latitudinal range of 50°–60°N. In this study, we focus on the clockwise branch of the AMOC, which is closely related to the deep convection in the North Atlantic, to make the discussion specifically and concisely.

To further compare the distinct structure of the AMOC in the two experiments, vertical structure of the AMOC at 26.5°N are compared. The observations from the Rapid Climate Change program (RAPID) data spanning from April 2004 to December 2014 (Cunningham et al. 2007) are also used here. The vertical profile of the AMOC and the seasonal variations of maximum meridional stream function at 26.5°N are plotted in Fig. 6. Consistent with the AMOC depicted in the latitude-depth diagram, the maximum transport of the AMOC is 17.4 Sv in STIF, which is comparable to the observation (16.8 Sv), while it is 14.9 Sv in CTRL (Fig. 6a). It is also evident that there is a deeper interface between the upper clockwise cell and lower counterclockwise cell in STIF, with the depth of 3.3 km, in contrast to 2.8 km in CTRL. Although the improvement on the depth of the southward deep flow is produced by using the "stiffened" EOS, it still suffers the deficiency with a shallower depth than the observed RAPID data (4.4 km). The shallower depth of the simulated AMOC probably caused by the excessive formation of the AABW compared to the observation (e.g., Liu et al. 2005) and the insufficient tidal mixing in the North Atlantic (Yu et al. 2017). Regarding the seasonal variations, both CTRL and STIF show similar tendency of variation except for a larger magnitude of the AMOC in STIF (Fig. 6b). Starting from May, STIF shows the same variations and magnitude as the RAPID data. However, larger values from January to April are seen in STIF, compared to the RAPID data.

3.2 Possible physical processes responsible for modification of the simulated AMOC

The dynamics and strength of the subpolar gyre, estimated by (10), in the North Atlantic determine the rate of deep-water formation (Katsman et al. 2004), which is closely associated with the deep convection and the AMOC. As shown in Fig. 7a, b, both CTRL and STIF capture the general features of the subtropical and subpolar gyres. However, compared to CTRL, there is a stronger subpolar gyre in the Labrador Sea and the Iceland–Scotland Basin in STIF (Fig. 7c). In addition, STIF shows larger potential density in the subpolar gyre (shading in Fig. 7c), compared to CTRL. The increased potential density corresponds to the intensified subpolar gyre
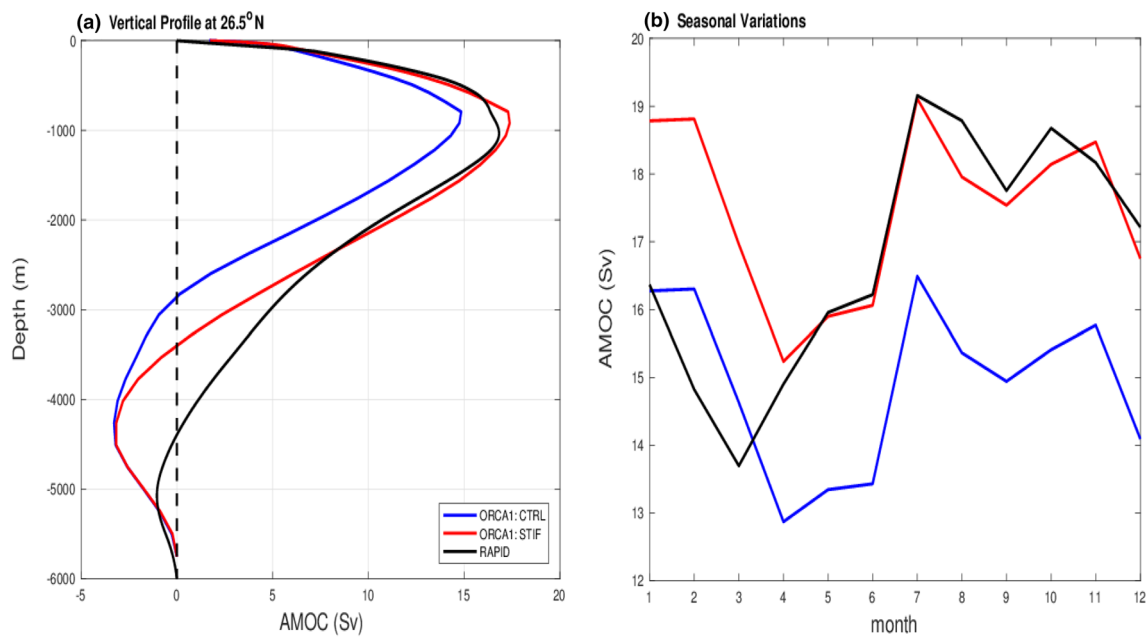
Fig. 6 a Vertical profiles of annual-mean meridional stream function (Sv) at 26.5°N and **b** seasonal variation of maximum meridional stream function (Sv) at 26.5°N of CTRL, STIF, and RAPID

in the Labrador Sea and the Iceland–Scotland Basin, which suggests that the subpolar gyre in part is controlled by the density (e.g., Häkkinen and Rhines 2004; Born et al. 2009).

It is considered that AMOC variability is modulated by the buoyancy forcing, which relates to the air-sea surface heat flux and freshwater flux, and wind forcing (e.g., Kuhlbrodt et al. 2007; Marshall et al. 2014). In the forced OGCM, however, Brankart (2013) pointed out that the forcing formulation produces an unrealistic spurious heat flux due to the lack of ocean feedback to adjust the atmosphere forcing. To avoid the confusion caused by the unrealistic heat flux, the buoyancy gain (B_{gain}) estimated by (9) is used in this study. The buoyancy gain resulted from the heat loss from ocean to atmosphere exerts an influence on the hydrographic features of sea water, especially at high polar latitudes (e.g., Yeager and Jochum 2009). Theoretic and numerical results have indicated that enhanced buoyancy gain leads to strong increase in stratification (Jansen and Nadeau 2016). Figure 8 depicts the annual-mean buoyancy gains in CTRL and STIF and their difference. Both CTRL and STIF, in general, produce similar distributions of the buoyancy gain (Fig. 8a, b). As shown by Fig. 8c, however, CTRL has a stronger stratification in the Labrador Sea, whereas STIF has a stronger stratification in the Irminger Sea. Additionally, the large buoyancy gain in STIF extends more eastward in the subtropical gyre. The difference between STIF and CTRL clearly illustrates that there is tremendous decrease of buoyancy gain in the Labrador Sea and on the south side of Iceland in STIF, implying that there is weaker stratification

in these regions in STIF. The stratification along the coastal region of the Greenland and the GIN seas is also reduced in STIF. However, the buoyancy gain in the Irminger Sea and the subtropical region is increased in STIF, enhancing the stratification. The reduced stratification in the Labrador Sea, the Iceland-Scotland Basin, and the GIN seas suggests that stronger deep convection, producing more deep water, occurs in these regions in STIF (Killworth 1983; Marshall and Schott 1999).

It is well known that intensified downwelling is accompanied by enhanced deep convection, though the two are not directly related to each other. The maximum mixed layer depth (MLD), which is often used to represent the occurrence of deep convection (e.g., Hu et al. 2008; Liu and Liu 2013; de Larvergne et al. 2014; Reintges et al. 2017), is first compared and discussed here. The MLD calculated in this study is defined as the depth at which the potential density differs from the surface value by 0.125 kg m^{-3}. Although estimate of the MLD, which can be defined by means of gradients or surface-to-depth differences of temperature, salinity, or density (e.g., Sprintall and Tomczak 1992; Anderson et al. 1996), over the global ocean is a complicated problem (Levitus 1982), the criterion and calculation used in this study is effective to represent the modeled mixed layer in the North Atlantic (e.g., Hosoda et al. 2010). Optimal estimate of the MLD is far beyond our scope in this study. Furthermore, the deep convection is supposed to occur at the place where the MLD is larger than 1000 m in this study. As shown in Fig. 9a, the deep convection in CTRL mainly
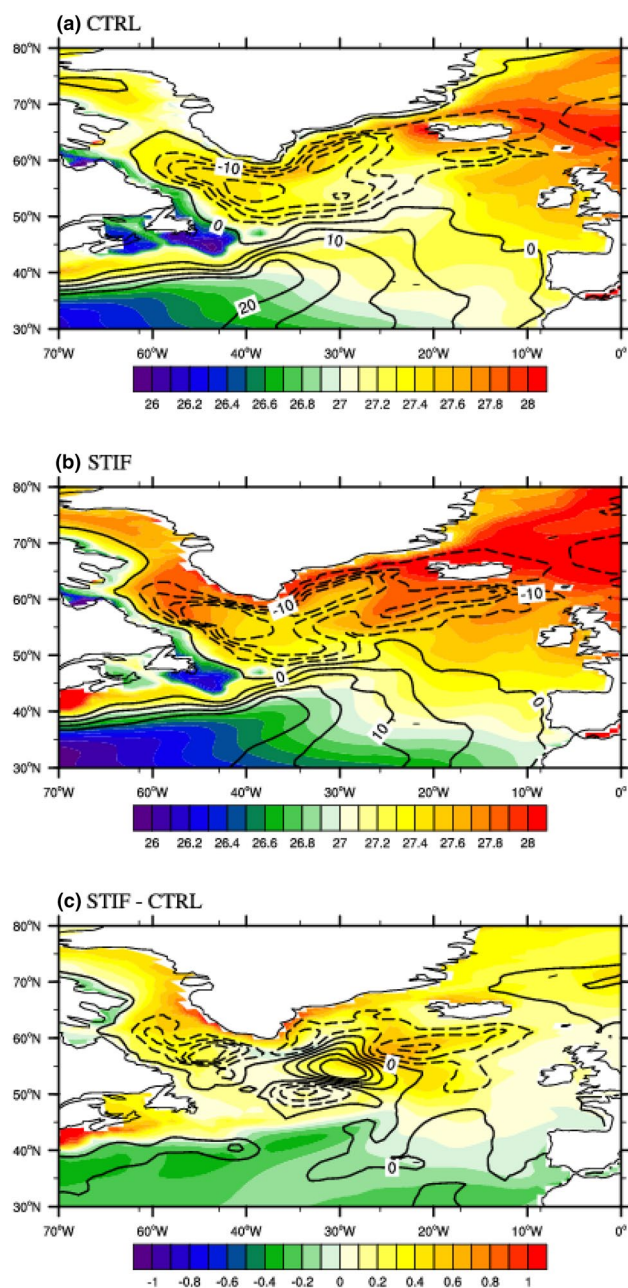
Fig. 7 Horizontal transport stream function (contour; Sv) and potential density (shading; kg m^{-3}) averaged over the upper 1000 m in DJF of **a** CTRL, **b** STIF, and **c** the difference between STIF and CTRL

Fig. 8 The buoyancy gain (m^2 s^{-2}) averaged in DJF of **a** CTRL, **b** STIF, and **c** the difference between STIF and CTRL

occurs in the Iceland Basin. However, there is a larger area where deep convection occurs in STIF (Fig. 9b). Enclosed by the black contour, the deep convection in STIF takes place in three different domains: the northern part of the Labrador Sea, the Irminger–Iceland–Scotland Basin, and the east side of the GIN seas. Based on hydrographic profiles of the World Ocean Circulation Experiment database and Argo floats, on the other hand, the deep convection is observed in the Labrador Sea during the boreal winter [refer to Fig. 5 in
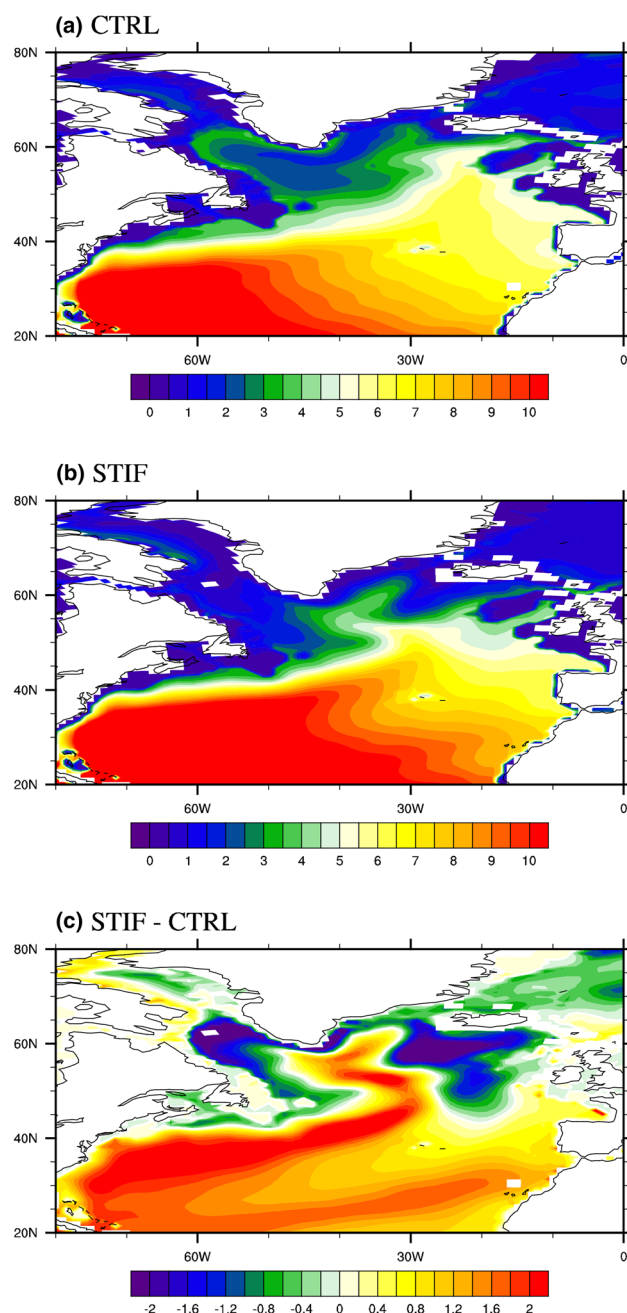
Montegut et al. (2004); Fig. 5a in Hosoda et al. (2010) for detail], though different definitions are used to calculate the MLD. Thus, more realistic deep convection is produced in STIF compared to CTRL. The distribution of MLD validates that there is stronger deep convection in STIF compared to CTRL.

Figure 10 shows the vertical profiles of mean temperature, salinity, potential density, and buoyancy frequency in DJF, which are area-averaged in the Labrador Sea
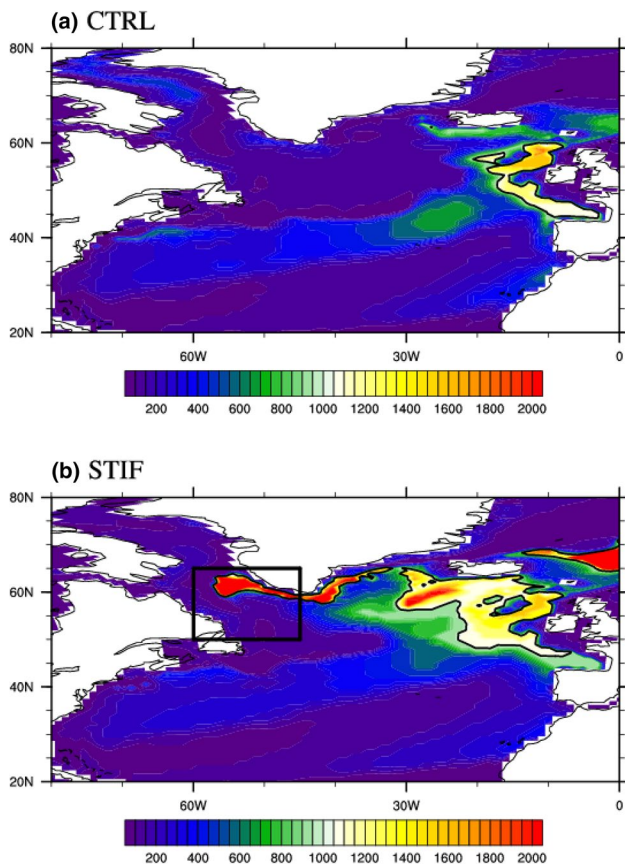
(a) CTRL

(b) STIF

Fig. 9 Maximum MLD (m) in March of **a** CTRL and **b** STIF. The thick black contour in **a** and **b** denotes the 1000-m isoline of the mixed layer depth. The thick black box in **b** denotes the Labrador Sea

(illustrated by the black box in Fig. 6b: and 50°N–65°N and 60°W–45°W). Compared to CTRL, STIF shows warmer seawater in the upper 300 m versus the colder sea water in the depth between 400 and 3000 m (Fig. 10a). As for salinity, it has similar vertical distribution with temperature (Fig. 10b). However, some minor differences exist, such as, saltier water in the upper 700 m in the Labrador Sea and fresher seawater between 700 and 2900 m in STIF compared to CTRL. STIF shows larger seawater density almost throughout the entire water depth (Fig. 10c). How does the buoyancy frequency, which is computed by $N^2 = -\frac{g}{\rho_0}\frac{\partial \rho}{\partial z}$, react to the change in density? As shown in Fig. 10d, STIF generally shows smaller buoyancy frequency in the entire water depth than CTRL, except in the upper 100 m. Focusing on the deep-convection region where the MLD is larger than 1000 m, the buoyancy frequency in STIF is much smaller than that in CTRL, especially in the upper 500 m and below 2500 m. The weakened stratification suggests the deep convection can take place more easily in STIF.

Thermobaricity ($\frac{\partial^2 \rho}{\partial \theta \partial p}$) and cabbeling ($\frac{\partial^2 \rho}{\partial \theta^2}$) induced by the nonlinearity of seawater EOS play central roles in the occurrence of deep convection in the polar oceans (e.g., Killworth 1979; Akitomo 1999). Both thermobaricity and cabbeling can cause vertical motion, which is inversely proportional to the buoyance frequency ($\propto N^{-2}$) (McDougall 1987). This kind of inverse relationship between vertical velocity and buoyance frequency suggests that the larger vertical velocity induced by thermobaricity and cabbeling is associated with weaker stratification of sea water. In addition, cabbeling always produces downwelling (negative vertical velocity); whereas thermobaricity produces either downwelling or upwelling depending on the sign of the dot product of gradients of potential temperature and pressure along the neutral surface. Note that the physical meaning of the density calculated by the "stiffened" EOS is intrinsically related to the thermobaricity (Dukowicz 2001). Thus, an expectation is that, compared to CTRL, STIF produces stronger thermobaricity as well as cabbeling, and induces larger vertical velocity. This can be seen in Fig. 11, which shows the DJF-mean vertical profiles of thermobaricity, cabbeling, and vertical velocity in the Labrador Sea (denoted as the black box in Fig. 9b: 60°W–45°W and 50°N–65°N). The intensified thermobaricity and cabbeling in STIF, especially in the deep ocean, produce larger vertical velocities compared to CTRL. Same analyses can be applied to the convective regions in the Irminger–Iceland–Scotland Basin and the GIN seas. The vertical profiles of potential density, buoyance frequency, cabbeling and thermobaric effects area-averaged over the Irminger–Iceland–Scotland Basin and the GIN seas illustrate similar physical properties as those in the Labrador Sea (Fig. S1 and S2).

3.3 Discussions

Previous studies have pointed out that disturbances of seawater hydrological properties in the tropical Atlantic potentially influence the variability of the AMOC (e.g., Zhang 2007; Mignot and Frankignoul 2010; Park et al. 2015). For example, positive salty anomaly produced in the tropical Atlantic is transported by the northward ocean currents, increasing the density and enhancing the deep convection in the North Atlantic (Mignot and Frankignoul 2010). Thus, purpose of the sensitivity experiment TALT_STIF is to investigate whether and how the changes in seawater properties in the tropical Atlantic affect the variability of the AMOC. On the other hand, as discussed in Sect. 3.2, the deep convection occurred in the North Atlantic, i.e., Labrador Sea, plays a vital role in enhancing the strength of AMOC. Therefore, another sensitivity experiment LABS_STIF is to confirm the importance of the deep convection occurred in the North Atlantic to the AMOC.

The difference of annual-mean AMOC between TALT_STIF and CTRL is shown in Fig. 12a. It is obvious that the usage of the "stiffened" EOS only in the tropical Atlantic
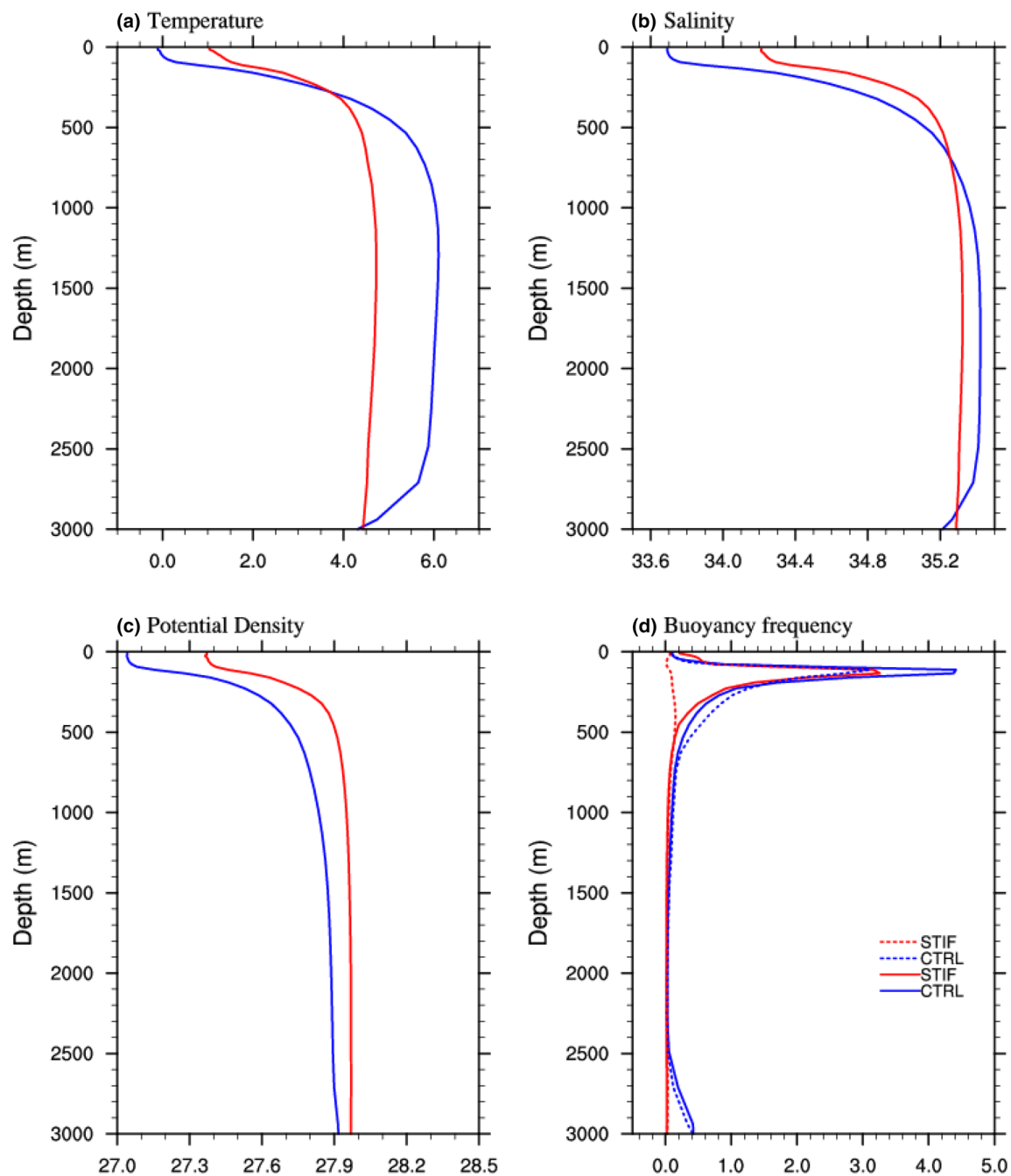
Fig. 10 Vertical profiles of **a** temperature (°C), **b** salinity (psu), **c** potential density (kg m^{-3}), and **d** buoyancy frequency (10^{-5} s^{-2}) area-averaged in the Labrador Sea (shown by the black box in Fig. 6b during the winter season (DJF). Blue and red lines represent the results of CTRL and STIF, respectively. The dashed lines in **d** represent the buoyancy frequency which are calculated in the areas where the MLD is deeper than 2000 m.

enhances the strength of the simulated AMOC. The differences of DJF-mean seawater temperature, salinity, and ocean currents averaged over the upper 200 m are also analyzed. Compared to CTRL, the temperature and salinity in TALT_STIF are decreased in the northern tropical Atlantic (Fig. 12b, c). In addition, increased temperature and salinity in TALT_STIF are found to extend southwestward from

Scotland basin to the regions of western boundary currents. In addition, the temperature and salinity in TALT_STIF are decreased in the subtropical gyre and Iceland basin. Regarding the ocean currents, as shown in Fig. 12d, the western boundary currents are enhanced in TALT_STIF compared to CTRL, which transport more warm and saline water northward to the Labrador sea making the sea water warmer and
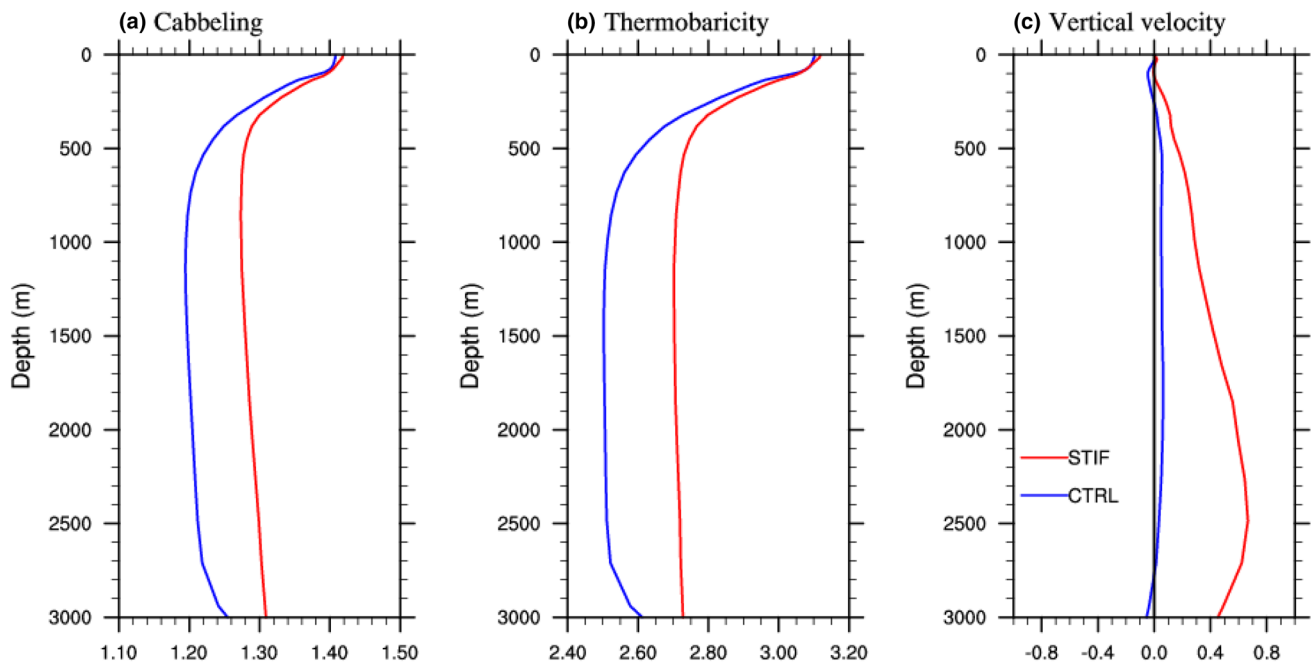
Fig. 11 Same as Fig. 10, except for **a** cabbeling (10^{-5} °C^{-2}), **b** thermobaricity [10^{-8} °C^{-1} (db)$^{-1}$], and **c** vertical velocity (m day^{-1}; positive for downward).

saltier there (Fig. 12b, c). The densification of sea water in the Labrador Sea enhances the deep convection and further intensifies the AMOC in TALT_STIF compared to CTRL (Mignot and Frankignoul 2010). Note that the differences in temperature and salinity between TALT_STIF and CTRL in the Irminger Sea are different from those between STIF and CTRL, suggesting that the processes leading to the enhanced AMOC are probably disparate between STIF and TALT_STIF.

Analogous results are obtained in the sensitivity experiment LABS_STIF (figure not shown), confirming that the deep convection in the Labrador Sea plays a vital role in the variability of the AMOC. The difference between LABS_STIF and TALT_STIF is shown in Fig. 13, aiming to compare the relative contribution to the variability of the AMOC. Compared to TALT_STIF, the clockwise branch of the AMOC is enhanced in LABS_STIF (Fig. 13a). In addition, the DJF-mean seawater temperature and salinity in the upper layer show large discrepancies in the Labrador and Irminger Seas. In the east and west coastal regions of the Greenland, where occurs the deep convection in STIF (Fig. 6), warmer and saltier water are found in LABS_STIF compare to TALT_STIF, whilst colder and fresher water are found in the southwest Labrador Sea (Fig. 13b, c). Moreover, the discrepancy of ocean currents with the order of cm s^{-1} between LABS_STIF and TALT_STIF is also found in the Labrador and Irminger Seas (Fig. 13d).

With respect to the sensitivity experiment SO_STIF, it shows different results from those of TALT_STIF and

LABS_STIF. As shown by Fig. 14a, the clockwise branch of the AMOC is weakened in SO_STIF with the minimum center during the depth range of 1000–2000 m compared to CTRL. Additionally, recalling the structure of the AMOC in CTRL (Fig. 5a), the anticlockwise branch of the AMOC is enhanced in SO_STIF, suggesting that more AABW is produced compared to CTRL. With respect to the temperature and salinity, the colder and fresher water are found in the Labrador and Irminger Seas in SO_STIF compared to CTRL (Fig. 14b, c). The weakened deep convection caused by the enhanced stratification in the Labrador and Irminger Seas further induces weakened AMOC. Moreover, difference of ocean currents indicates that weakened western boundary currents are produced in SO_STIF, which relates to the northward transports of warm and salty water from low latitudes to high latitudes and finally influences the AMOC (Fig. 14d).

Concluding from aforementioned discussions, the physical processes responsible for the effects of the "stiffened" EOS on the improvement in simulating the AMOC can be summarized in a schematic diagram (Fig. 15). Incorporation of the "stiffened" EOS first induces denser surface water and enhances the subpolar gyre, which induces weakened stratification and intensified thermobaric effect and cabbeling. These give rise to enhanced deep convection with larger vertical velocity; as a consequence, an intensified AMOC occurs. In turn, the intensified AMOC enhances the strength of northward surface return flow, increasing the meridional heat and salt transports, contributing to the densification of surface water.
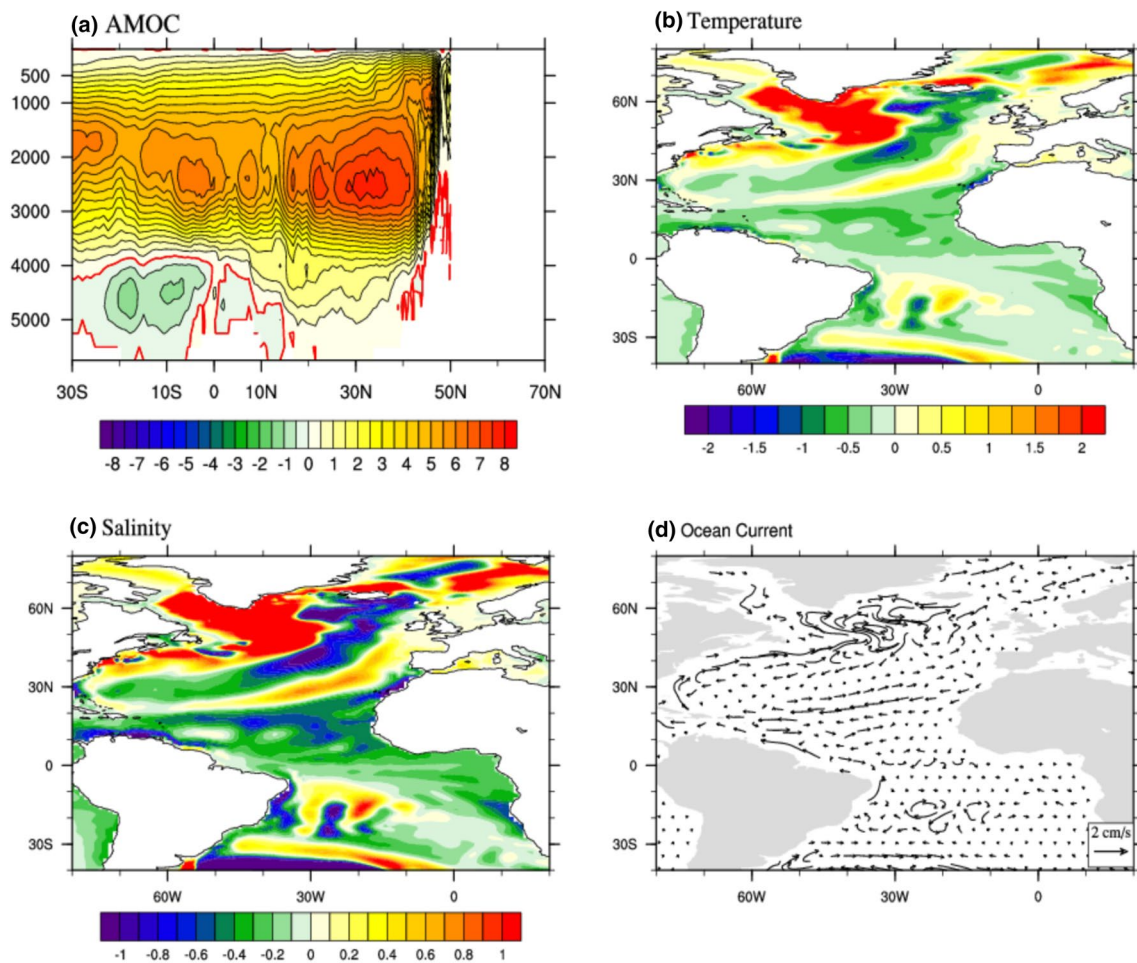
Fig. 12 Difference of **a** annual-mean meridional stream function (Sv), and DJF-mean, **b** temperature (°C) and **c** salinity (psu), and **d** ocean currents (cm s⁻¹) between TALT_STIF and CTRL. The tem-perature, salinity, and ocean currents are averaged over the upper 200 m. Red curve in **a** denotes the zero isoline.

4 Summary and concluding remarks

Two seawater EOSs, the standard EOS (CTRL) and "stiff-ened" EOS (STIF), are used in OGCM NEMO3.4 to explore their impacts on simulated AMOC in this study. Results show that, compared to CTRL, the SST and SSS in the northeast Labrador Sea, the Irminger Sea, and the GIN seas are increased in STIF. In addition, the meridional heat transport in the Atlantic is enhanced in STIF, which is mainly attributed to the overturning heat transport south of 50°N and the gyre heat transport north of 50°N. Moreover, STIF performs better in simulating the AMOC, including its strength and spatial structure. The vertical profile at 26.5°N further confirms the improvements in STIF in simulating the AMOC; especially, the maximum strength of AMOC in STIF is comparable to the observation.

The MLD in March indicates that the deep convection in STIF takes place in the Labradors Sea, the

Irminger-Iceland-Scotland Basin, and the GIN seas, while that in CTRL only occurs in the Iceland Basin. Meanwhile, there is larger MLD in STIF, suggesting that stronger deep convection occurs in STIF compared to CTRL. The distribution of buoyancy gain indicates that the static stability is weakened in the Labrador Sea, Irminger-Iceland Basin, and the GIN seas in STIF, which are the regions prone to deep convection. In addition, the vertical profiles of temperature and salinity in the Labrador Sea illustrate that the temperature and salinity in the upper ocean are increased in STIF and decreased in the deep ocean, leading to the increase in the potential density in the entire water column. The changes in potential density increase the meridional gradient of potential temperature, which contributes to the intensification of the subpolar gyre in STIF. Moreover, the strengthened thermobaricity and cabbeling weaken the stratification, suggesting stronger deep convection is generated there in STIF, as reflected by the deeper MLD in March.
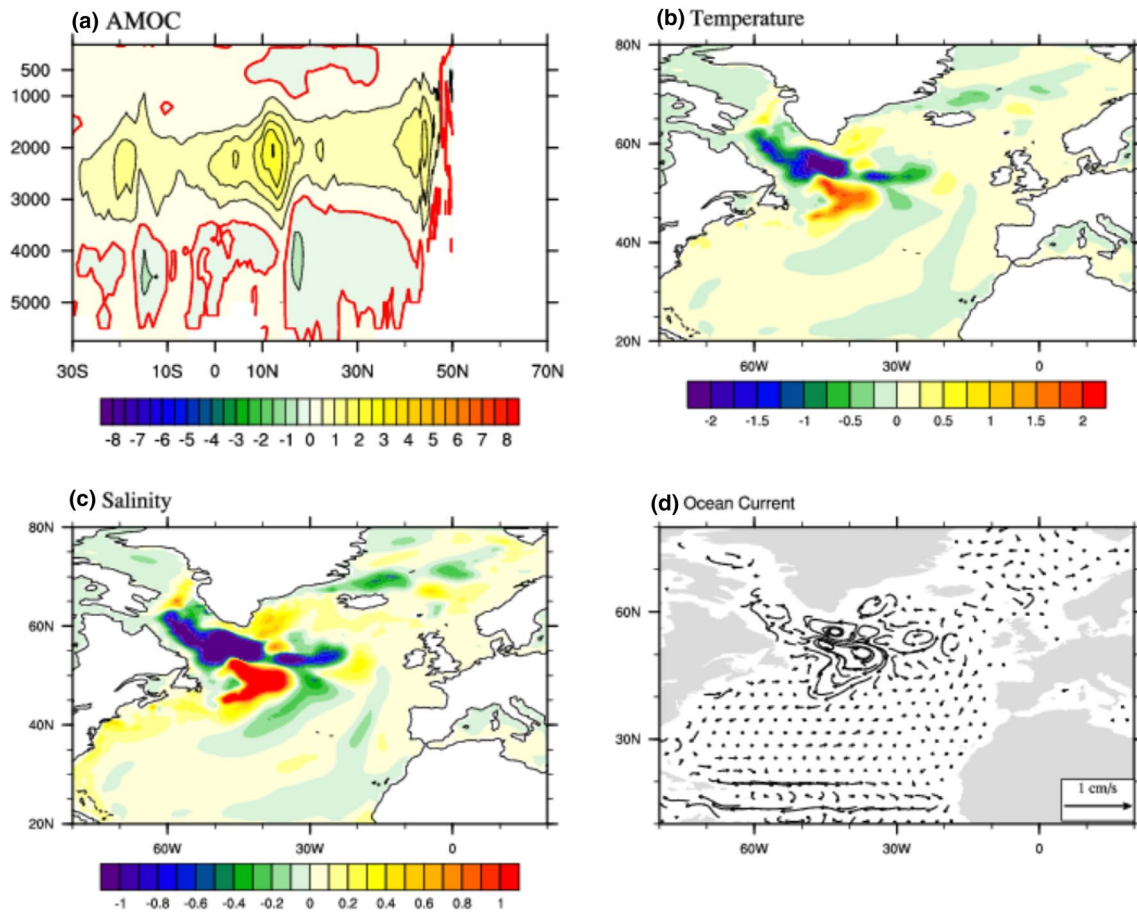
Fig. 13 Same as in Fig. 12 but for the difference between LABS_STIF and TALT_STIF.

The physical processes responsible for better performance of STIF in simulating the AMOC compared to CTRL are also examined in this study, which includes both direct and indirect causes. The usage of "stiffened" EOS first increases the density from the upper to the deep ocean up to 3000 m, which can modify the stability of sea water. The smaller buoyance frequency implies that the deep convection occurs more easily in STIF. The densification of seawater with increases (decreases) of temperature and salinity in the upper (deep) ocean intensifies the cabbeling and thermobaric effect, which strengthen vertical advection; thus, there are enhanced deep convection and formation of deep water in STIF compared to CTRL. The increased formation of deep water eventually improves the simulated AMOC in terms of strength and depth. The enhanced AMOC, in turn, speeds up the surface return flow, which crosses the equator and moves from low to high latitudes in the North Atlantic. As a result, more warm and saline surface water is transported to the high latitudes by the strengthened surface currents, generally causing warmer and more saline surface water in the subpolar gyre in STIF compared to CTRL.

In this work, although the simulated AMOC is improved in STIF, it still suffers some deficiencies. In terms of the vertical profile at 26.5°N, the upper cell in STIF is still shallower compared to RAPID. Moreover, regarding the seasonal variation of the maximum AMOC at 26.5°N, there are smaller annual range and larger magnitude of the AMOC from January to April in STIF. This suggests that other physical processes also attribute to the AMOC, such as tidal mixing, which is needed for further investigation in the future. On the other hand, without additional restoring of SSS leads to the drift in salinity because of the uncertainties of precipitation forcing, which possibly impacts the results obtained in this study. With the insight gained from this study, thus, we will apply the "stiffened" EOS to NESMv3, in which no fluxes correction are applied, to investigate its impacts on the simulation of the AMOC and to explore whether it has influence on the decadal and multidecadal variation of the AMOC and the associated climate variability.
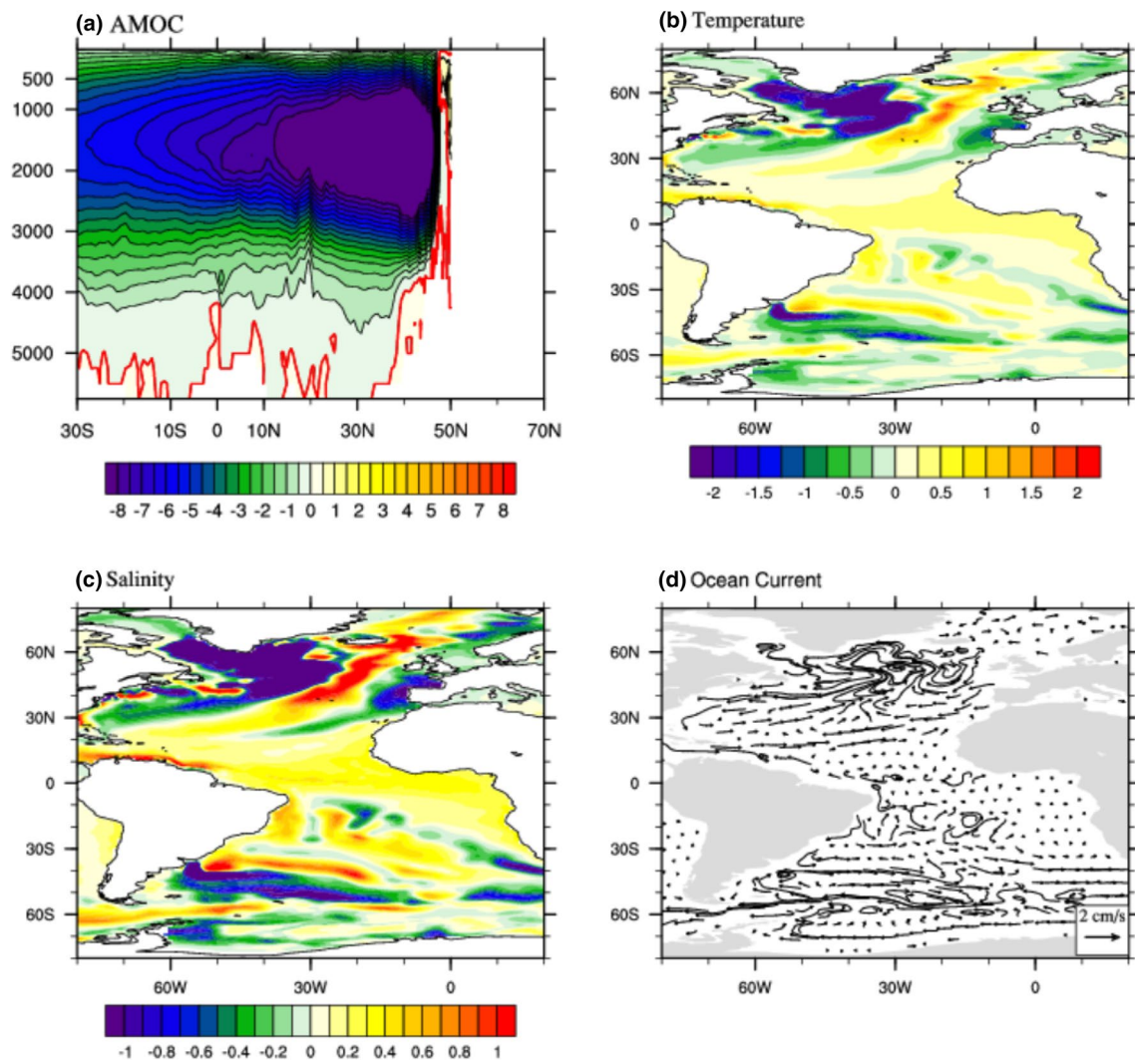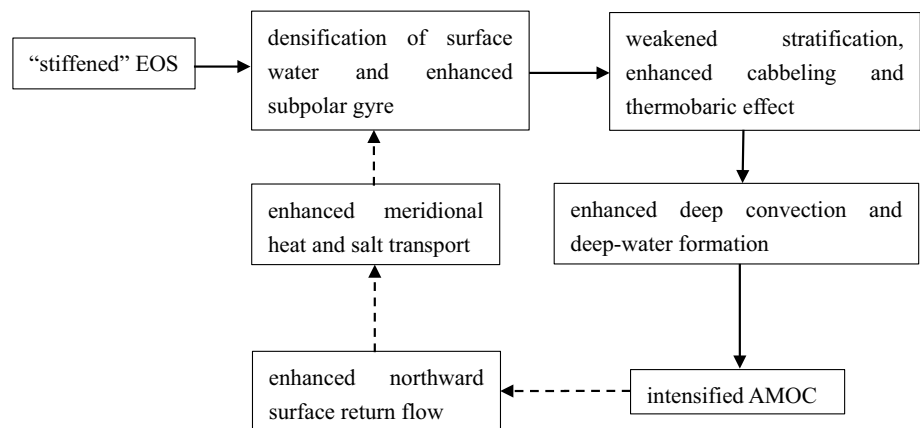
Fig. 14 Same as in Fig. 12 but for the difference between SO_STIF and CTRL.

Fig. 15 Schematic diagram representing the physical processes responsible for the improvement of simulated AMOC by using the "stiffened" EOS. The solid (dashed) arrows denote the direct (indirect) cause.

"stiffened" EOS

densification of surface water and enhanced subpolar gyre

weakened stratification, enhanced cabbeling and thermobaric effect

enhanced meridional heat and salt transport

enhanced deep convection and deep-water formation

enhanced northward surface return flow

intensified AMOC

References

Akitomo K (1999) Open-ocean deep convection due to thermobaricity 1. Scaling argument. J Geophys Res 104:5225–5234

Alley RB et al (2003) Abrupt climate change. Science 299:2005–2010

Anderson SP, Weller RA, Lukas RB (1996) Surface buoyancy forcing and the mixed layer of the western pacific warm pool: observations and 1d model results. J Clim 9(12):3056–3085

Behrens E, Biastoch A, Böning CW (2013) Spurious AMOC trends in global ocean sea-ice models related to subartic freshwater forcing. Ocean Modell 69:39–49

Blanke B, Delecluse P (1993) Variability of the tropical Atlantic Ocean simulated by a general circulation model with two different mixed-layer physics. J Phys Oceanogr 23:1363–1388

Boon JD (2012) Evidence of sea level acceleration at US and Canadian tide stations, Atlantic Coast, North America. J Coast Res 28:1437–1445

Born A, Levermann A, Mignot J (2009) Sensitivity of the Atlantic Ocean circulation to a hydraulic overflow parameterization in a coarse resolution model: response of the subpolar gyre. Ocean Model 27:130–142

Born A, Nisancioglu KH, Braconnot P (2010) Sea ice induced changes in ocean circulation during the Eemian. Clim Dyn 35:1361–1371

Brankart J-M (2013) Impact of uncertainties in the horizontal density gradient upon low resolution global ocean modelling. Ocean Model 66:64–76

Bryden HL, Imawaki S (2001) Ocean heat transport. In: Siedler G, Church J, Gould J (eds) Ocean circulation and climate: observing and modelling the global ocean. Acdemic Press, San Diego, pp 455–474

Cao J, Wang B, Yang YM, Ma LB et al (2018) The NUIST Earth System Model (NESM) version 3: Description and preliminary evaluation. Geosci Model Dev 11:2975–2993

Chen C, Liu W, Wang G (2019) Understanding the uncertainty in the 21st century dynamic sea level projections: The role of the AMOC. Geophys Res Lett 46:210–217

Cheng WC, Bitz CM, Chiang JCH (2007) Adjustment of the global climate to an abrupt slowdown of the Atlantic meridional overturning circulation, in ocean circulation: mechanisms and impacts-past and future changes of Meridional overturning. AGU, Washington DC, pp 295–313

Cunningham SA et al (2007) Temporal variability of the Atlantic meridional overturing circulation at 26.5°N. Science 317:935–938

Danabasoglu G et al (2014) North Atlantic simulations in coordinated ocean-ice reference experiments phase II (CORE-II). Part I: mean states. Ocean Model 73:76–107

Danabasoglu G et al (2016) North Atlantic simulations in Coordinated Ocean-ice Reference Experiments phase II (CORE-II). Part II: Inter-annual to decadal variability. Ocean Model 97:65–90

de Boyer Montegut C, Madec G, Fischer AS et al (2004) Mixed layer depth over the global ocean: An examination of profile data and a profile-based climatology. J Geophy Res 109:C12003. https://doi.org/10.1029/2004JC002378

de Lavergne C, Palter JB, Galbraith ED, Bernardello R, Marinov I (2014) Cessation of deep convection in the open southern ocean under anthropogenic climate change. Nat Clim Change 4:278–282

Delworth TL et al (2012) Simulated climate and climate change in the GFDL CM2.5 high-resolution coupled climate model. J Clim 25:2755–2781

Deshayes J, Curry R, Msadek R (2014) CMIP5 model intercomparison of freshwater budget and circulation in the North Atlantic. J Clim 27:3298–3317

Dewar WK, Hsueh Y, McDougal TJ, Yuan DY (1998) Calculation of pressure in ocean simulations. J Phys Oceanogr 28:577–588

Drews A, Greatbatch RJ, Ding H, Latif M, Park W (2015) The use of a flow field correction technique for alleviating the North Atlantic cold bias with application to the Kiel Climate Model. Ocean Dyn 65:1079–1093

Dukowicz JK (2001) Reduction of density and pressure gradient errors in ocean simulations. J Phys Oceanogr 31:1915–1921

Dussin R, Barnier B (2013) The making of DFS 5.1. Drakkar Project Rep, p 40

Ezer T (2013) Sea level rise, spatially uneven and temporally unsteady: Why the U.S. east coast, the global tide gauge record, and the global altimeter data show different trends. Geophys Res Lett 40:5493–5444

Fichefet T, Maqueda MM (1997) Sensitivity of a global sea ice model to the treatment of ice thermodynamics and dynamics. J Geophys Res 102:609–646

Frierson DMW, Hwang YT, Fuckar NS (2013) Contribution of ocean overturning circulation to tropical rainfall peak in the Northern Hemisphere. Nat Geosci 6:940–944

Fofonoff NP, Millard RD (1983) Algorithms for computation of fundamental properties of seawater. UNESCO Marine Science Tech Paper, vol 44, p 55

Gao YQ, Drange H, Bentsen M (2003) Effect of diapycnal mixing and isopycnal mixing on the ventilation of CFCs in the North Atlantic in an isopycnal coordinate OGCM. Tellus B 55:837–854

Gent PR, McWilliams JC (1990) Isopycnal mixing in ocean circulation models. J Phys Oceanogr 20:150–155

Gill AF (1982) Atmosphere-ocean dynamics. Academic, New York, p 662

Griffies SM et al (2009) Coordinated ocean-ice reference experiments (COREs). Ocean Model 26:1–46

Häkkinen S, Rhines PB (2004) Decline of subpolar North Atlantic circulation during the 1990s. Science 309:1841–1844

Hosoda S, Ohira T, Sato K, Suga T (2010) Improved description of global mixed-layer depth using Argo profiling floats. J Oceanogr 66:773–787

Hu A, Otto-Bliesner BL, Meehl GA et al (2008) Response of thermohaline circulation to freshwater forcing under present day and LGM conditions. J Clim 21:2239–2258

Hurrel JW et al (2013) The community earth system model: a framework for collaborative research. Bull Am Meteor Soc 94:1339–1360

Jackett DR, McDougall TJ (1995) Minimal adjustment of hydrographic profiles to achieve static stability. J Atmos Ocean Technol 12:381–389

Jansen M, Nadeau L-P (2016) The effect of Southern Ocean surface buoyance loss on the deep-ocean circulation and stratification. J Phys Oceanogr 45:3455–3470

Karspeck AR et al (2017) Comparison of the Atlantic meridional overturning circulation between 1960 and 2007 in six ocean reanalysis products. Clim Dyn 49:957–982

Katsman C, Spall M, Pickart R (2004) Boundary current eddies and their role in the restratification of the Labrador Sea. J Phys Oceanogr 34:1967–1983

Kevin I et al (2005) Can limited mixing buffer rapid climate change. Tellus A 57:676–690

Killworth PD (1979) On "Chimney" formations in the ocean. J Phys Oceanogr 9:531–554

Killworth PD (1983) Deep convection in the world ocean. Rev Geophys Space Phys 21:1–26

Kopp RE et al (2010) The impact of Greenland melt on local sea levels: A partially coupled analysis of dynamic and static equilibrium effects in idealized water-hosing experiments. Clim Change 103:619–625

Kuhlbrodt T, Griesel A, Montoya M, Levermann A, Hofmann M, Rahmstorf S (2007) On the driving processes of the Atlantic meridional overturning circulation. Rev Geophys 45:RG2001

Large WG, Yeager S (2004) Diurnal to decadal global forcing for ocean and sea-ice models: the datasets and flux climatologies. NCAR Tech. Note, NCAR/TN-460 + STR, CGD Division of the National Center for Atmospheric Research

Levermann A, Griesel A, Hofmann M, Montoya M, Rahmstorf S (2005) Dynamic sea level changes following changes in the thermohaline circulation. Clim Dyn 24:347–354

Levitus S (1982) Climatological Atlas of the world ocean. NOAA/ERL GFDL Professional Paper 13. Princeton

Liu W, Hu A (2015) The role of the PMOC in modulating the deglacial shift of the ITCZ. Clim Dyn 45:3019–3034

Liu W, Liu Z (2013) A diagnostic indicator of the stability of the Atlantic Meridional Overturning Circulation in CCSM3. J Clim 26:1926–1938

Liu W, Xie SP, Liu Z, Liu J (2017) Overlooked possibility of a collapsed Atlantic Meridional Overturning Circulation in warming climate. Sci Adv 3:e1601666. https://doi.org/10.1126/sciadv.1601666

Liu Z, Shin S, Webb R et al (2005) Atmospheric CO2 forcing on glacial thermohaline and climate. Geophys Res Lett 32:L02706. https://doi.org/10.1029/2004GL021929

Lozier MS (2012) Overturning in the North Atlantic. Annu Rev Mar Sci 4:291–315

Luyten J, McCartney M, Stommel H (1993) On the sources of North Atlantic Deep Water. J Phys Oceanogr 23:1885–1891

Lynch-Stieglitz J et al (2007) Atlantic overturning circulation during the last glacial maximum. Science 316:66–69

Madec G (2008) Nemo ocean engine. http://www.nemo-ocean.eu

Marshall J, Donohoe A, Ferreira D, McGee D (2014) The ocean's role in setting the mean position of the Inter-Tropical Convergence Zone. Clim Dyn 42:1967–1979

Marshall J, Schott F (1999) Open-ocean convection: Observations, theory, and models. Rev Geophys 37:1–64

Marzocchi A, Hirschi JJ-M et al (2015) The North Atlantic subpolar circulation in an eddy-resolving global ocean model. J Mar Syst 142:126–143

McCarthy GD, Haigh ID, Hirschi JJ, Grist JP, Smeed DA (2015) Ocean impact on decadal Atlantic climate variability revealed by sea-level observations. Nature 521:508–510

McDougall TJ (1987) Thermobaricity, cabbelling, and water-mass conversion. J Geophys Res 92:5448–5464

McManus JF et al (2004) Collapse and rapid resumption of Atlantic meridional circulation lined to deglacial climate changes. Nature 428:834–836

Mignot J, Frankignoul C (2010) Local and remote impacts of a tropical Atlantic salinity anomaly. Clim Dyn 35:1133–1147

Park AO, SchmIDt MW, Chang P (2015) Tropical North Atlantic subsurface warming events as a fingerprint for AMOC variability during Marine Isotope Stage 3. Paleoceaography 30:1425–1436

Rahmstorf S (2002) Ocean circulation and climate during the past 120,000 years. Nature 419:207–214

Redi MH (1982) Oceanic isopycnal mixing by coordinate rotation. J Phys Oceanogr 12:1154–1158

Sallenger AH, Doran KS, Howd P (2012) Hotspot of accelerated sea-level rise on the Atlantic coast of North America. Nat Clim Change. https://doi.org/10.1038/NCILMATE1597

Shchepetkin AF, McWilliams JC (2011) Accurate Boussinesq oceanic modeling with a practical, "stiffened" equation of state. Ocean Model 38:41–70

Smith R et al (2010) The Parallel Ocean Program (POP) reference manual: Ocean component of the Community Climate System Model (CCSM) and Community Earth System Model (CESM). Los Alamos National Laboratory Tech Rep LAUR-10-01853

Sprintall J, Tomczak M (1992) Evidence of the barrier layer in the surface layer of the tropics. J Geophys Res 97:7305–7316

Srokosz MA et al (2012) Past, present, and future changes in the Atlantic Meridional Overturning Circulation. Bull Am Meteorol Soc 93:1663–1676

Srokosz MA, Bryden HL (2015) Observing the Atlantic Meridional Overturning Circulation yields a decade of inevitable surprises. Science. https://doi.org/10.1126/science.1255575

Stammer D (2008) Response of the global ocean to Greenland and Antarctic ice melting. J Geophys Res. https://doi.org/10.1029/2006JC004079

Stammer D, Agarwal N, Herrmann P, Kohl A, Mechoso CR (2011) Response of a coupled ocean-atmosphere model to Greenland ice melting. Surv Gepphys 32:621–642

Reintges A, Martin T, Latif M, Park W (2017) Physical controls of Southern Ocean deep-convection variability in CMIP5 models and the Kiel Climate Model. Geophys Res Lett 44(13):6951–6958

Timmermann A et al (2007) The influence of a weakening of the Atlantic Meridional Overturning Circulation on ENSO. J Clim 20:4899–4918

UNESCO (1981) Background papers and supporting data on the international Equation of State of seawater 1980. Unesco technical papers in marine science

Vellinga M, Wood R (2002) Global climatic impacts of a collapse of the Atlantic thermohaline circulation. Clim Change 54:251–267

Yashayaev I, Bersch M, van Aken HM (2007) Spreading of the Labrador Sea Water to the Irminger and Iceland basins. Geophys Res Lett 34:L10602. https://doi.org/10.1029/2006GL028999

Yeager YG, Jochum M (2009) The connection between Labrador Sea buoyance loss, deep western boundary current strength, and Gulf Stream path in an ocean circulation model. Ocean Model 30:207–224

Yin J, Schlesinger ME, Stouffer RJ (2009) Model projections of rapID sea level rise on the northeast coast of the United States. Nat Geosci 2:262–266

Yu ZP, Liu HL, Lin PF (2017) A numerical study of the influence of tIDal mixing on Atlantic merIDional overturning circulation (AMOC) simulation. Chin J Atmos Sci (in Chinese) 41:1087–1100

Zeytounian RK (2003) Joseph Boussinesq and his approximation: a contemporary view. C R Mecanique 331:575–586

Zhang R (2007) Anticorrelated multidecadal variations between surface and subsurface tropical North Atlantic. Geophys Res Lett 34:L12713. https://doi.org/10.1029/2007GL030225

Zhang R, Delworth TL (2005) Simulated tropical response to a substantial weakening of the Atlantic thermohaline circulation. J Clim 18:1853–1860